

See discussions, stats, and author profiles for this publication at: <https://www.researchgate.net/publication/263962105>

Synthesis and Photoelectrochemical Properties of $(\text{Cu}_2\text{Sn})_x\text{Zn}_{3(1-x)}\text{S}_3$ Nanocrystal Films

ARTICLE in THE JOURNAL OF PHYSICAL CHEMISTRY C · MAY 2014

Impact Factor: 4.77 · DOI: 10.1021/jp500270d

CITATIONS

3

READS

49

7 AUTHORS, INCLUDING:



Chi-Hung Chuang

University of Colorado Boulder

20 PUBLICATIONS 478 CITATIONS

SEE PROFILE



Liejin Guo

Xi'an Jiaotong University

340 PUBLICATIONS 8,239 CITATIONS

SEE PROFILE



Clemens Burda

Case Western Reserve University

173 PUBLICATIONS 14,921 CITATIONS

SEE PROFILE

Synthesis and Photoelectrochemical Properties of $(\text{Cu}_2\text{Sn})_x\text{Zn}_{3(1-x)}\text{S}_3$ Nanocrystal Films

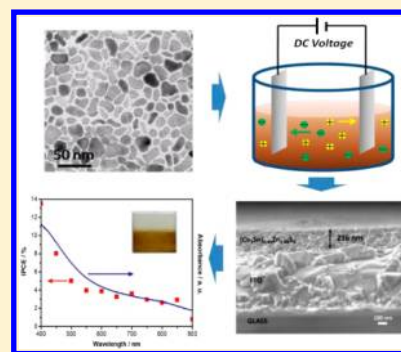
Yubin Chen,^{†,‡} Chi-Hung Chuang,[‡] Keng-Chu Lin,[‡] Shaohua Shen,[†] Christopher McCleese,[‡] Liejin Guo,^{*,†} and Clemens Burda^{*,‡}

[†]International Research Center for Renewable Energy, State Key Laboratory of Multiphase Flow in Power Engineering, Xi'an Jiaotong University, Shaanxi 710049, P. R. China

[‡]Center for Chemical Dynamics and Nanomaterials Research, Department of Chemistry, Case Western Reserve University, 10900 Euclid Avenue, Cleveland, Ohio 44106, United States

S Supporting Information

ABSTRACT: This work provides new routes for developing efficient photoelectrodes for photoelectrochemical (PEC) water splitting using a low-cost electrophoretic film preparation method. A series of $(\text{Cu}_2\text{Sn})_x\text{Zn}_{3(1-x)}\text{S}_3$ ($0 \leq x \leq 0.75$) quaternary nanocrystals (NCs) with tunable optical band gaps are synthesized. Morphologies including particles, rods, and wires are obtained by tuning the composition of the NCs. $(\text{Cu}_2\text{Sn})_{0.75}\text{Zn}_{0.75}\text{S}_3$ ($\text{Cu}_2\text{ZnSnS}_4$) has a pure kesterite structure, but an increase in the Zn content results in a kesterite–wurtzite polytypism. $(\text{Cu}_2\text{Sn})_x\text{Zn}_{3(1-x)}\text{S}_3$ films are fabricated from their colloidal solutions via electrophoretic deposition, and the PEC properties of these films with p-type character have been examined under water-splitting conditions. It is shown that the photocurrent varies as a function of film thickness as well as chemical composition. The produced $(\text{Cu}_2\text{Sn})_{0.45}\text{Zn}_{1.65}\text{S}_3$ ($x = 0.45$) film has the highest photocurrent, and the incident photon to current conversion efficiency is improved compared with previously reported results of $\text{Cu}_2\text{ZnSnS}_4$ photocathodes.



INTRODUCTION

Since the first report on photodissociation of water by Fujishima and Honda,¹ clean hydrogen production through photoelectrochemical (PEC) water splitting has attracted considerable attention with regard to aspects of renewable and sustainable energy solutions. Different kinds of semiconductors have been explored and considered as photoelectrodes for solar water splitting,^{2–7} but in terms of practical applications semiconductor electrodes necessitate high efficiency, long-term stability, low cost, and low toxicity.

Devices using III–V semiconductors have shown conversion efficiencies above 10%, but their applications are limited due to poor corrosion resistance and high cost.^{8,9} Most metal oxide photoelectrodes on the other hand are stable and inexpensive,^{10–14} but PEC performances are typically limited by poor light-absorption efficiency, low carrier mobility, and short diffusion lengths.^{15,16} Copper-based chalcogenide films have been widely used for solar cells with high efficiency and long-term stability due to narrow band gaps, high absorption coefficients, and practical carrier transport properties.¹⁷ Recently copper-based chalcogenide (e.g., CuInS_2 , CuGa_3Se_5 , and $\text{Cu}(\text{In,Ga})\text{Se}_2$) films were used as photocathodes for PEC water splitting and have been shown to be potential materials for such applications.^{18–21}

Among the various copper-based chalcogenides, the p-type semiconductor $\text{Cu}_2\text{ZnSnS}_4$ (CZTS) has been considered as one of the most promising light-absorbing materials for thin film solar cells due to its high absorption coefficient ($>10^4 \text{ M}^{-1}$

cm^{-1}), suitable band gap ($\sim 1.5 \text{ eV}$), low toxicity, and elemental abundance.^{22,23} Power conversion efficiencies of 7.3% and 8.4% have been obtained for CZTS solar cells,^{24,25} and an efficiency of 11.1% has been reached by partly replacing S with Se.²⁶ Several groups have discussed the PEC properties of CZTS in the presence of electron scavengers; however, related studies using CZTS photocathodes for water splitting were rarely carried out.^{27–29} Domen's group reported using CZTS deposited onto Mo coated soda-lime glass substrates by way of magnetron cosputtering for water splitting. Although the efficiency of these photocathodes was rather high with modification of CdS and Pt, the incident photon to current conversion efficiency (IPCE) was only 0.01% at 600 nm under an applied potential of -0.24 V vs a reversible hydrogen electrode (RHE).^{30,31} Sivula's group has recently reported the optimization and stabilization of electrodeposited CZTS photocathodes for solar-powered water reduction. However, efficient PEC activity could only be achieved by coupling the photocathode with Pt and CdS.³² In terms of large-scale applications it is desirable to avoid high cost and the use of potentially toxic materials; therefore, developing efficient CZTS-based photoelectrodes in the absence of Pt and Cd is of great significance. Kudo and co-workers have used a series of stannite-type complex sulfides such as $\text{A}_2^{\text{I}}\text{–Zn–A}^{\text{IV}}\text{–S}_4$ ($\text{A}^{\text{I}} =$

Received: January 9, 2014

Revised: May 5, 2014

Published: May 7, 2014



Cu and Ag; $A^{IV} = \text{Sn}$ and Ge) for photocatalytic hydrogen generation, and it was found that the photocatalytic activities depend on their chemical composition.³³ Ford et al. synthesized $\text{Cu}_2\text{Zn}(\text{Sn}_{1-x}\text{Ge}_x)\text{S}_4$ nanocrystals (NCs) with a $\text{Ge}/(\text{Ge}+\text{Sn})$ ratio of 0.7 yielding an efficiency of 6.8% for solar cell applications.³⁴ The results from this study suggest that the PEC performance of CZTS-based NCs can be influenced by their composition. In addition, Zhan's group reported the synthesis of composition-adjustable $(\text{Cu}_2\text{Sn})_{x/3}\text{Zn}_{1-x}\text{S}$ nanoparticles with tunable band gaps.³⁵ The great potential of $(\text{Cu}_2\text{Sn})_{x/3}\text{Zn}_{1-x}\text{S}$ nanoparticles for photoelectric energy conversion was revealed by their implementation in quantum dot sensitized solar cells, and different efficiencies were obtained by varying the x values. Similarly $(\text{ZnS})_x(\text{Cu}_2\text{SnS}_3)_{1-x}$ NCs have also been prepared by Liu et al.³⁶ Torimoto et al. demonstrated that the PEC properties of $\text{Cu}-\text{Zn}-\text{Sn}-\text{S}$ quaternary semiconductors in the presence of electron scavengers depended on their chemical composition, especially on the Cu/Sn ratio in the NCs.³⁷ It was reported that quaternary $\text{Cu}_2\text{SnZnS}_4$ (CZTS) is derived from ZnS by substituting Zn with Cu and Sn ions.³⁸ Therefore, it is reasonable to form a series of CZTS-based compounds by tuning the $\text{Zn}/(\text{Cu}+\text{Sn})$ ratio, which can be denoted as $(\text{Cu}_2\text{Sn})_x\text{Zn}_{3(1-x)}\text{S}_3$. When the x value equals 0.75, it forms CZTS. These CZTS-based materials are of particular interest for PEC applications because their optical properties and structural parameters can be tuned by simply controlling the synthesis ratios between copper, zinc, and tin, possibly leading to the enhanced PEC activity compared to CZTS.

In this study we present a two-step solution-based technique to fabricate $(\text{Cu}_2\text{Sn})_x\text{Zn}_{3(1-x)}\text{S}_3$ films. First, a series of $(\text{Cu}_2\text{Sn})_x\text{Zn}_{3(1-x)}\text{S}_3$ ($0 \leq x \leq 0.75$) NCs are synthesized by a hot-injection method, and quaternary compounds were successfully achieved. With varying composition the $(\text{Cu}_2\text{Sn})_x\text{Zn}_{3(1-x)}\text{S}_3$ NCs showed different optical band gaps, morphologies, and crystal structures. Second, an electrophoretic deposition (EPD) method is applied to prepare $(\text{Cu}_2\text{Sn})_x\text{Zn}_{3(1-x)}\text{S}_3$ films from their colloidal solutions. The EPD method is based on the movement of charged particles in solution under a dc electric field followed by NC deposition onto oppositely charged electrodes. This process forms homogeneous microstructures with low surface roughness.³⁹ EPD has the advantages of simplicity, low cost, and high deposition rate. This method has been employed to fabricate various semiconductor films including those of CdSe , TiO_2 , and BiVO_4 .^{40–43} Although the preparation of CZTS films by way of EPD was recently reported by Kornhuber,⁴⁴ a series of $(\text{Cu}_2\text{Sn})_x\text{Zn}_{3(1-x)}\text{S}_3$ films prepared by this method has never been reported. The PEC properties of the prepared films were then examined under water-splitting conditions. $(\text{Cu}_2\text{Sn})_x\text{Zn}_{3(1-x)}\text{S}_3$ NC films with different compositions and varied activities have been synthesized. The best efficiency was obtained for the $(\text{Cu}_2\text{Sn})_{0.45}\text{Zn}_{1.65}\text{S}_3$ film where x equals 0.45.

EXPERIMENTAL SECTION

Chemicals. Copper(II) acetate monohydrate ($\text{Cu}(\text{OAc})_2 \cdot \text{H}_2\text{O}$, Fisher Scientific, 99%), zinc acetate dihydrate ($\text{Zn}(\text{OAc})_2 \cdot 2\text{H}_2\text{O}$, Aldrich, 99%), tin(IV) chloride pentahydrate ($\text{SnCl}_4 \cdot 5\text{H}_2\text{O}$, Aldrich, 98%), sulfur powder (S , Aldrich, 99.5%), oleylamine (OLE, Aldrich, 90%), hexane (Fisher Scientific, 99.9%), and isopropyl alcohol (Fisher Scientific, 99.9%) were used as purchased without further purification.

Synthesis of $(\text{Cu}_2\text{Sn})_x\text{Zn}_{3(1-x)}\text{S}_3$ Nanocrystals. The quaternary $(\text{Cu}_2\text{Sn})_x\text{Zn}_{3(1-x)}\text{S}_3$ NCs of varying compositions were prepared by a hot-injection method as described in the literature with the following modifications.³⁶ First, 1.6 mmol of total metal salts ($\text{Cu}(\text{OAc})_2 \cdot \text{H}_2\text{O}$, $\text{SnCl}_4 \cdot 5\text{H}_2\text{O}$, and $\text{Zn}(\text{OAc})_2 \cdot 2\text{H}_2\text{O}$ in a stoichiometric molar ratio) and 20.0 mL of OLE were loaded in a 50 mL three-necked round-bottom flask. In this reaction OLE acts as both the solvent and the capping ligand for the NCs. The reaction flask was heated up to 135 °C and kept under vacuum for 120 min in order to remove oxygen and water. After evacuation, the flask was filled with Ar (g) and heated to 245 °C. The S-OLE solution (1.6 mmol of S dissolved in 2 mL of OLE) was rapidly injected into the flask with vigorous stirring at 245 °C. After 60 min of growth, the reaction was terminated by removing the heating mantle. After the mixture reached room temperature, isopropyl alcohol was added and the solution was centrifuged for 10 min to precipitate the NCs. The quaternary NCs were finally dispersed in 30 mL of hexane for the following measurements and characterization.

Preparation of $(\text{Cu}_2\text{Sn})_x\text{Zn}_{3(1-x)}\text{S}_3$ Electrodes. $(\text{Cu}_2\text{Sn})_x\text{Zn}_{3(1-x)}\text{S}_3$ films were prepared by EPD of $(\text{Cu}_2\text{Sn})_x\text{Zn}_{3(1-x)}\text{S}_3$ NCs onto fluorine-doped tin oxide (FTO) coated glass substrates (Hartford Glass TEC 8 with sheet resistance of 8 Ω/square). First, excess OLE was removed by washing with isopropyl alcohol. The washed NCs were dispersed in 20 mL of hexane for EPD. In a typical EPD process two pieces of FTO glass were immersed in the colloidal solution with a separation distance of 1 cm, and a dc voltage of 210 V was applied for 10 min by a Keithley 2400 sourcemeter. The glass electrodes were then rinsed with ethanol, dried with compressed air, and ready for PEC experiments. By repeating the EPD process, the number of deposition layers of $(\text{Cu}_2\text{Sn})_x\text{Zn}_{3(1-x)}\text{S}_3$ NCs could be increased.

Characterization. UV-visible absorption spectra were recorded using a Varian Cary 50 spectrometer. The morphology of the NCs was characterized with a JEOL 1200CX transmission electron microscope (TEM, operating at an accelerating voltage of 80 kV). The crystal structure was examined by a Scintag X-1 Advanced X-ray powder diffractometer ($\text{Cu K}\alpha$ radiation). The Raman scattering study was performed on a Jobin Yvon LabRAM HR spectrometer using 514.5 nm irradiation (20 mW) from an Ar^+ laser. Elemental composition of the prepared NCs was determined by a Noran energy dispersive X-ray spectroscopy (EDX) system attached to a Hitachi S4500 field-emission scanning electron microscope (FESEM). The morphology and film thickness were analyzed with a JEOL JSM-7800F FESEM.

Photoelectrochemical Measurements. The PEC performances of the prepared electrodes were examined in a three-electrode cell with a saturated calomel electrode (SCE) as a reference electrode and a platinum wire as a counter electrode. A 0.1 M Na_2SO_4 aqueous solution (pH adjusted to 3 by using H_2SO_4) was used as the electrolyte. A scanning potentiostat (CH Instruments, model CHI 630) was used to measure photocurrents under chopped irradiation from a 150 W Xe lamp (Newport) equipped with an AM 1.5 filter. In order to facilitate the analysis, all potentials vs SCE were converted to the RHE scale according to the Nernst equation presented in eq 1 where E_{RHE} is the converted potential vs RHE, $E_{\text{SCE}}^\theta = 0.2415 \text{ V}$ at 25 °C, and E_{SCE} is the experimentally measured potential against a SCE reference.

$$E_{\text{RHE}} = E_{\text{SCE}} + 0.059\text{pH} + E_{\text{SCE}}^{\theta} \quad (1)$$

IPCE measurements were carried out using a home-built system. Broad solar illumination from a 150 W Xe lamp was directed into a monochromator (Chromex 250), and the absolute incident light intensity from the monochromator was measured with a power meter (Coherent Fieldmate) while the photocurrent was monitored with a CHI 630 potentiostat. The IPCE was calculated using eq 2 where I is the photocurrent density, λ is the incident light wavelength, and J is the measured incident irradiance.

$$\text{IPCE} = \frac{1240 \times I}{\lambda J} \quad (2)$$

RESULTS AND DISCUSSION

Optical Properties. UV–vis absorption spectra of the prepared $(\text{Cu}_2\text{Sn})_x\text{Zn}_{3(1-x)}\text{S}_3$ NCs in hexane are shown in Figure 1. These spectra display broad absorption features. The

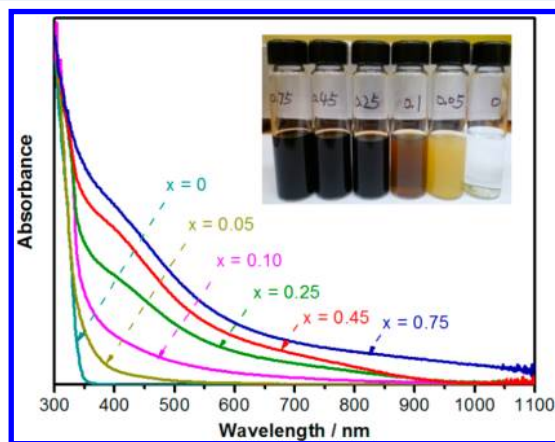


Figure 1. UV–vis absorption spectra of $(\text{Cu}_2\text{Sn})_x\text{Zn}_{3(1-x)}\text{S}_3$ NCs in hexane. When $x = 0$, it results in binary ZnS NCs with absorption below 400 nm. Increasing Cu and Sn content leads to quaternary NCs with absorption ranging from 300 to 1100 nm. The inset shows prepared $(\text{Cu}_2\text{Sn})_x\text{Zn}_{3(1-x)}\text{S}_3$ NC solutions under room light with increasing x values (from right to left).

absence of sharp exciton bands are typical in ternary and quaternary NCs.^{35,45} Upon increasing the zinc content (decreasing x value), the absorption gradually blue-shifts, as shown in Figure 1, signifying an increasing optical band gap. The tunable band gap of the prepared $(\text{Cu}_2\text{Sn})_x\text{Zn}_{3(1-x)}\text{S}_3$ NCs indicates that a series of quaternary NCs is obtained by changing the chemical composition. Since both ZnS ($x = 0$) and CZTS ($x = 0.75$) are direct-gap semiconductors, $(\text{Cu}_2\text{Sn})_x\text{Zn}_{3(1-x)}\text{S}_3$ NCs with varying x values are also considered as direct-gap semiconductor materials.³⁵ Pure ZnS absorbs light only in the UV region, while the CZTS ($x = 0.75$) absorption covers the UV, visible, and near-infrared regions. The broad absorption spectrum of CZTS makes it a desirable semiconductor material for light-harvesting applications.

The optical band gap of the prepared $(\text{Cu}_2\text{Sn})_x\text{Zn}_{3(1-x)}\text{S}_3$ NCs can be determined by extrapolating the linear portion of the $(\alpha h\nu)^2$ vs $h\nu$ plots (Figure 2a–f) where α is the optical absorption coefficient and $h\nu$ is the photon energy.⁴⁶ Summarized in Table 1, the band gaps for $(\text{Cu}_2\text{Sn})_x\text{Zn}_{3(1-x)}\text{S}_3$ NCs are between 1.51 and 3.9 eV. The CZTS NCs with the highest Cu and Sn content have a band gap of 1.51 eV which is

in agreement with the experimentally reported value²³ and slightly less than the theoretical value of 1.64 eV.⁴⁷ As discussed below, there are likely crystallographic defects present in these NCs due to nonstoichiometric amounts of ions, and this slight deviation from 1.64 eV may be explained by these defects. Pure ZnS NCs have a band gap of 3.9 eV which is in accordance with the reported value for wurtzite ZnS (3.7–3.9 eV).⁴⁸ The photograph of the colloidal solutions (inset in Figure 1) shows that increasing the zinc content (lowering x) changes the color from dark brown, to brownish red, to yellow, and finally to colorless which is in agreement with the increasing band gap. The colloidal solutions are optically clear and stable for NCs with x values above 0.10. However, solutions with high Zn content, such as $(\text{Cu}_2\text{Sn})_{0.1}\text{Zn}_{2.7}\text{S}_3$ ($x = 0.10$) and $(\text{Cu}_2\text{Sn})_{0.05}\text{Zn}_{2.85}\text{S}_3$ ($x = 0.05$), are less stable, and some precipitation was observed several days after the synthesis.

Figure 3 shows the band gap of the NCs as a function of chemical composition. Included in the figure is a range of reported values for the band gap of Cu_2SnS_3 (CTS, $x = 1$).⁴⁹ It is clear from Figure 3 that the NC band gap is strongly dependent on the chemical composition of the material, including band gap bowing. The variation of the band gap with chemical composition is likely due to the formation of polymorphs and defects present in the NCs both of which are further discussed later in this work.

NC Size and Shape. The morphology of the synthesized quaternary NCs was investigated with TEM. Figure 4a shows that CZTS NCs have a spherulike shape with a diameter of ~ 12 nm. Upon increasing zinc content, rodlike (Figure 4b and 4c) and wirelike (Figure 4d) shapes are formed. It is worth noting that increasing Zn content not only increased the aspect ratio but repeatedly changed the curvature of the NC as well. The curved shape becomes dominant for NCs with more Zn ($x = 0.10$). Compared with nanoparticles and nanorods, $(\text{Cu}_2\text{Sn})_{0.1}\text{Zn}_{2.7}\text{S}_3$ nanowires tend to agglomerate and precipitate from the colloidal solution. When the Zn content is further increased, a mixture of large aggregates and small NCs can be found as shown in Figure 4e. The small NCs in Figure 4e have a similar size (~ 3 nm) as the synthesized pure ZnS NCs in Figure 4f. $(\text{Cu}_2\text{Sn})_{0.05}\text{Zn}_{2.85}\text{S}_3$ ($x = 0.05$) has an estimated band gap of 2.75 eV (Table 1), which should be ascribed to the large aggregates. This band gap is larger than those for $(\text{Cu}_2\text{Sn})_x\text{Zn}_{3(1-x)}\text{S}_3$ ($0.10 \leq x \leq 0.75$) and smaller than that for ZnS. Therefore, the $(\text{Cu}_2\text{Sn})_{0.05}\text{Zn}_{2.85}\text{S}_3$ in Figure 4e is inferred to consist of aggregated quaternary NCs and small ZnS NCs.

The lattice stability of the quaternary NCs gradually decreases with increasing zinc content in $(\text{Cu}_2\text{Sn})_x\text{Zn}_{3(1-x)}\text{S}_3$. As the zinc content exceeds a critical amount, the excess zinc will form ZnS. Quaternary NCs with varying morphologies are obtained only in the ranges of $x = 0.75$ – 0.10 . Figure 4g shows that decreasing the x value leads to slight reduction in the diameter of the NCs (from 11.5 to 7.7 nm) and a great increase in length (from 11.5 to 100 nm). Thus, morphological transitions are achieved for $(\text{Cu}_2\text{Sn})_x\text{Zn}_{3(1-x)}\text{S}_3$ NCs by tuning the chemical compositions. A report on $\text{CuIn}_x\text{Ga}_{1-x}\text{S}_2$ semiconductors found that transitions in the morphology are attributed to the ability of the cation to coordinate differently with the solvent, and this too may explain the transitions seen in the NCs prepared in this work.⁵⁰

Crystal Structure. Figure 5a shows the XRD patterns of $(\text{Cu}_2\text{Sn})_x\text{Zn}_{3(1-x)}\text{S}_3$ NCs with different compositions. Different crystal structures are obtained and tabulated in Table 1. The

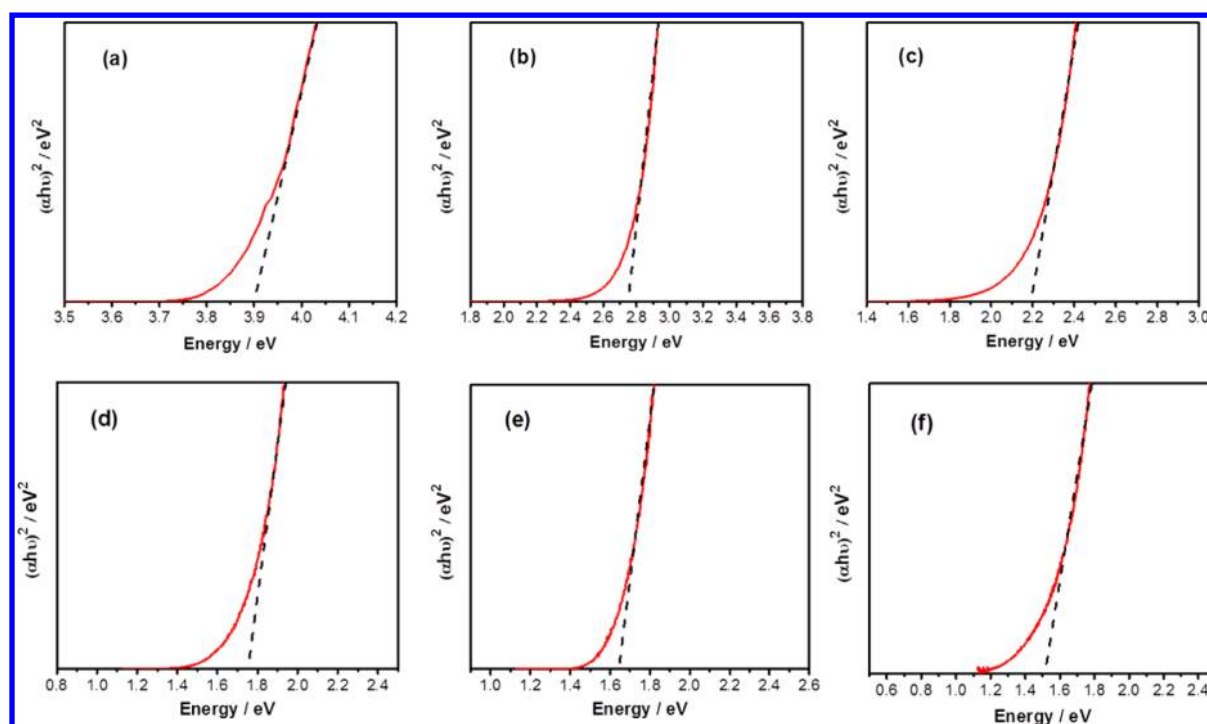


Figure 2. Plots in red of $(\alpha h\nu)^2$ vs photon energy ($h\nu$) for $(\text{Cu}_2\text{Sn})_x\text{Zn}_{3(1-x)}\text{S}_3$ NCs with different x values: (a) $x = 0$, (b) $x = 0.05$, (c) $x = 0.10$, (d) $x = 0.25$, (e) $x = 0.45$, and (f) $x = 0.75$.

Table 1. Band gap (E_g), Diameter (D), and Crystalline Phase of $(\text{Cu}_2\text{Sn})_x\text{Zn}_{3(1-x)}\text{S}_3$ NCs with Varying x Values^a

x	E_g/eV	D/nm	phase
0.75	1.51	11.7	k
0.45	1.64	11.6	k
0.25	1.75	13.2	k
0.1	2.19	17	k/w
0.05	2.75	24.2	k/w-ZnS
0	3.9	3.1	w-ZnS

^a E_g is the optical band gap from Figure 2, D is the diameter of the NC determined by Scherrer's equation from XRD, and k stands for the kesterite phase, k/w for kesterite/wurtzite polytypes, and w-ZnS for wurtzite ZnS.

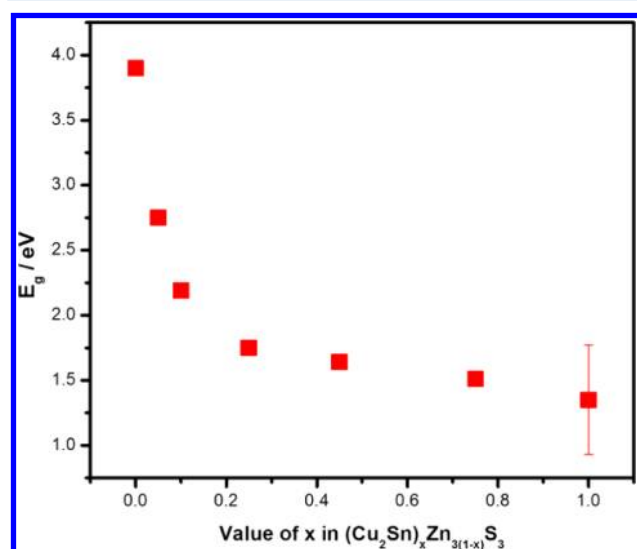


Figure 3. Band gap as a function of chemical composition.

diffraction peaks for CZTS ($x = 0.75$) observed at 2θ values of 28.39° , 32.79° , 47.24° , and 56.05° could be indexed to those of kesterite CZTS (JCPDS no. 26-0575).^{22,51} The kesterite phase is derived from zinc-blende ZnS by substituting Zn with Cu and Sn ions.³⁸ Pure ZnS ($x = 0$) has weak and broad diffraction peaks due to the small crystalline size of ~ 3 nm, and these peaks align with those of a wurtzite structure (JCPDS no. 80-0007) instead of a zinc blende structure.⁵² The XRD pattern of $(\text{Cu}_2\text{Sn})_{0.1}\text{Zn}_{2.7}\text{S}_3$ ($x = 0.10$) reveals that the kesterite phase is dominant while three small peaks are observed at 2θ values of 26.99° , 30.41° , and 51.68° which are contributed by a wurtzite phase.^{51,53} These results demonstrate that a kesterite–wurtzite polytypism occurs in $(\text{Cu}_2\text{Sn})_{0.1}\text{Zn}_{2.7}\text{S}_3$. Although the wurtzite phase was not clearly identified in both $(\text{Cu}_2\text{Sn})_{0.45}\text{Zn}_{1.65}\text{S}_3$ ($x = 0.45$) and $(\text{Cu}_2\text{Sn})_{0.25}\text{Zn}_{2.25}\text{S}_3$ ($x = 0.25$) NCs, very weak peaks of the wurtzite phase at a 2θ value of $\sim 27.00^\circ$ were observable.

CZTS ($x = 0.75$) has a stable kesterite structure while pure ZnS ($x = 0$) has a wurtzite structure. It is expected that atoms would rearrange to form the wurtzite phase with decreasing x values as in $(\text{Cu}_2\text{Sn})_{0.1}\text{Zn}_{2.7}\text{S}_3$ ($x = 0.10$). For $(\text{Cu}_2\text{Sn})_{0.05}\text{Zn}_{2.85}\text{S}_3$ ($x = 0.05$) NCs, the XRD pattern exhibits the typical diffraction peaks of kesterite phase and a broad peak overlaps with the main peak ($2\theta = 28.60^\circ$) of the kesterite phase which was indexed to that of wurtzite ZnS. This suggests that a mixture of kesterite quaternary NCs and wurtzite ZnS is obtained in $(\text{Cu}_2\text{Sn})_{0.05}\text{Zn}_{2.85}\text{S}_3$ ($x = 0.05$). The crystalline sizes of $(\text{Cu}_2\text{Sn})_x\text{Zn}_{3(1-x)}\text{S}_3$ NCs were calculated using Scherrer's equation shown in Table 1. Increasing Zn content results in the large crystalline size except for pure ZnS which has a size of ~ 3.1 nm which is in good agreement with the TEM results.

The Raman spectra of $(\text{Cu}_2\text{Sn})_x\text{Zn}_{3(1-x)}\text{S}_3$ ($0.10 \leq x \leq 0.75$) NCs were examined to further investigate these structures. As shown in Figure 5b, the Raman peaks at 331 cm^{-1} indicate the existence of CZTS close to previously reported value.⁵⁴ No additional Raman peaks for ZnS (352 cm^{-1}), SnS_2 (315 cm^{-1}),

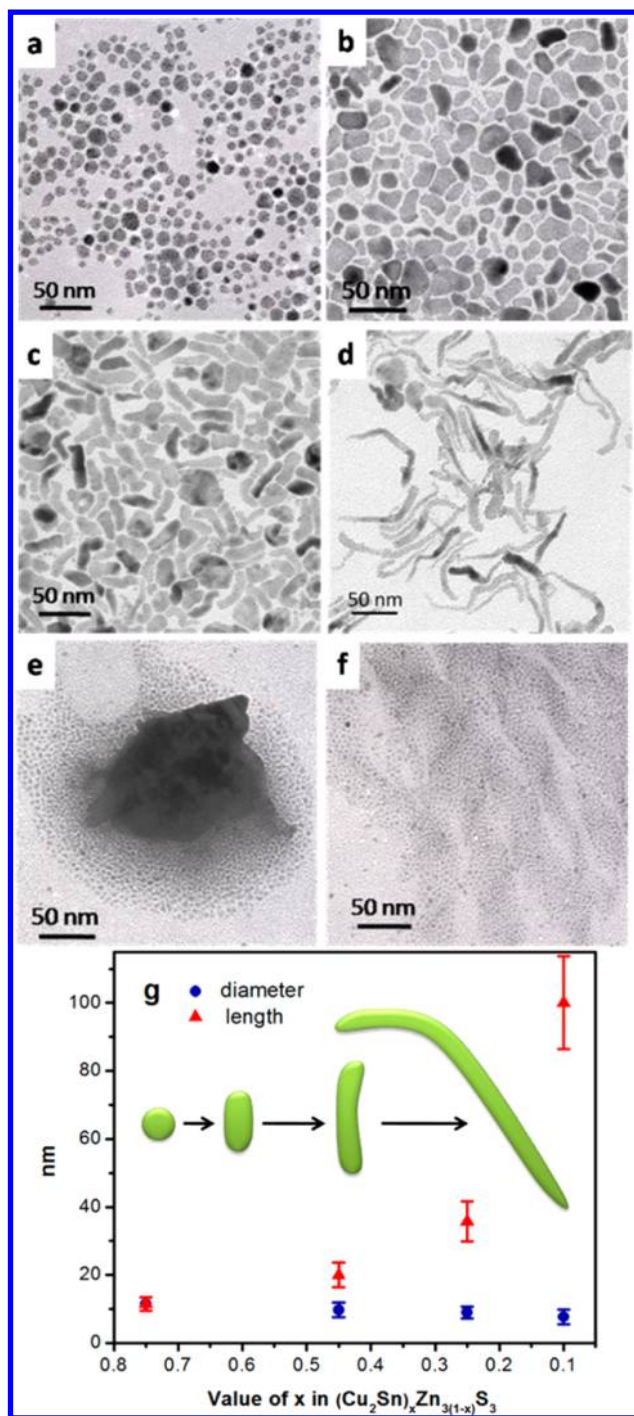


Figure 4. TEM images of $(\text{Cu}_2\text{Sn})_x\text{Zn}_{3(1-x)}\text{S}_3$ NCs with decreasing x values: (a) $x = 0.75$, (b) $x = 0.45$, (c) $x = 0.25$, (d) $x = 0.10$, (e) $x = 0.05$, and (f) $x = 0$. The scale bar is 50 nm in each TEM image. The dimensions of different $(\text{Cu}_2\text{Sn})_x\text{Zn}_{3(1-x)}\text{S}_3$ NCs and their morphologic transition from $x = 0.75$ to 0.10 (green scheme from left to right) are shown in (g). The dimensions are estimated by examining more than 50 NCs.

or Cu_2S (472 cm^{-1}) were observed indicating the absence of impurities.⁵⁴ With decreasing x value, the Raman peaks for $(\text{Cu}_2\text{Sn})_x\text{Zn}_{3(1-x)}\text{S}_3$ ($0.10 \leq x \leq 0.75$) NCs gradually shift to higher wavenumbers. Similarly, their diffraction peaks at the 2θ value of $\sim 28.39^\circ$ slightly shift toward higher angle in Figure 5a. However, the diffraction peak shift is quite small, due to the similar ionic radii of Cu^+ , Sn^{4+} , and Zn^{2+} .³⁵ The Raman and

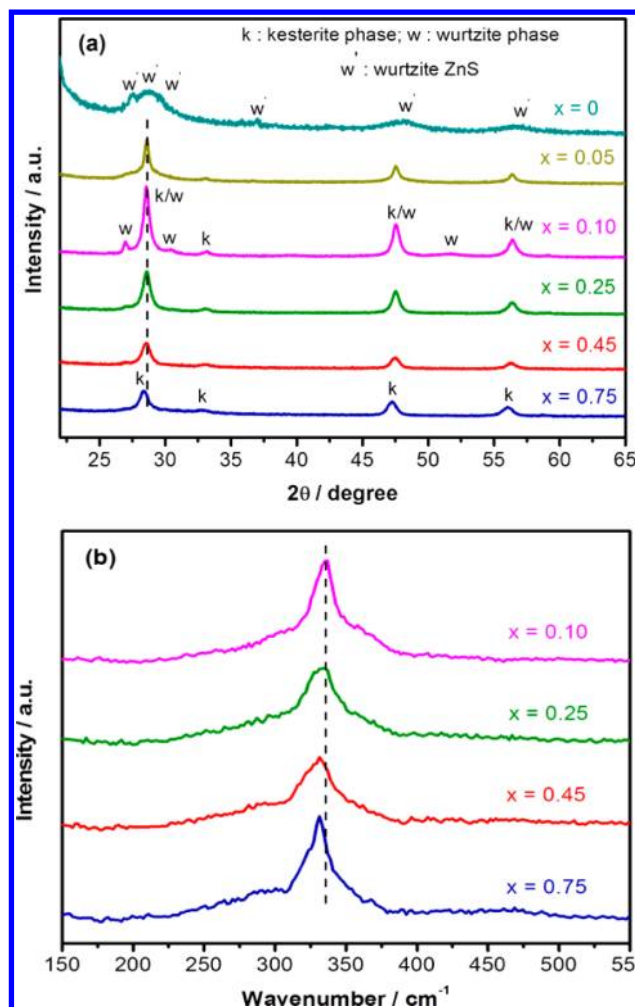


Figure 5. (a) XRD patterns of $(\text{Cu}_2\text{Sn})_x\text{Zn}_{3(1-x)}\text{S}_3$ NCs with different x values. When $x = 0.10$, the NCs are kesterite–wurtzite polytypism. The peak intensity of ZnS ($x = 0$) is magnified five times for clarity. (b) Raman spectra of $(\text{Cu}_2\text{Sn})_x\text{Zn}_{3(1-x)}\text{S}_3$ NCs with varying Zn content.

XRD peak shifts indicate a gradual change in the structure of $(\text{Cu}_2\text{Sn})_x\text{Zn}_{3(1-x)}\text{S}_3$ ($0.10 \leq x \leq 0.75$) NCs with altered composition, which further demonstrates that a series of $(\text{Cu}_2\text{Sn})_x\text{Zn}_{3(1-x)}\text{S}_3$ NCs has been successfully synthesized.

Deviations in Composition. The elemental compositions of $(\text{Cu}_2\text{Sn})_x\text{Zn}_{3(1-x)}\text{S}_3$ ($0.10 \leq x \leq 0.75$) NCs were examined by energy dispersive X-ray spectroscopy (EDX). As shown in Figure 6a, the composition variations of the different samples are in good agreement with the changes of their stoichiometric ratios. Decreasing the x value has resulted in the increase of Zn while the amount of sulfur remained constant. All samples were sulfur-deficient compared to their stoichiometric ratios. This deficiency could be due to sulfur vaporization during injection into a hot solution.

Nonstoichiometric compositions were observed for all samples. Herein, the composition deviation of $(\text{Cu}_2\text{Sn})_x\text{Zn}_{3(1-x)}\text{S}_3$ is defined as the summation of the deviation from each element, which can be calculated by eq 3 where D is the deviation for the element and C_{EDX} and C_{stoich} are the atomic concentration from EDX measurements and the chemical formula, respectively.

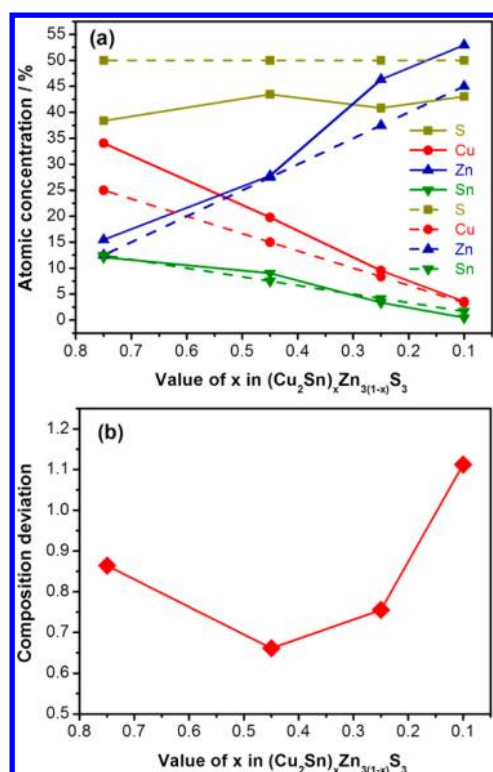


Figure 6. (a) Relative elemental compositions determined by EDX (solid line) and stoichiometry formula (dashed line) of $(\text{Cu}_2\text{Sn})_x\text{Zn}_{3(1-x)}\text{S}_3$ NCs. (b) The composition deviation of $(\text{Cu}_2\text{Sn})_x\text{Zn}_{3(1-x)}\text{S}_3$ NCs. The EDX measurements were carried out in an area of $7 \times 7 \mu\text{m}^2$. Every sample was examined three times in different regions.

$$D = \left| \frac{C_{\text{EDX}} - C_{\text{stoich}}}{C_{\text{stoich}}} \right| \quad (3)$$

The composition deviations are displayed in Figure 6b with $(\text{Cu}_2\text{Sn})_{0.45}\text{Zn}_{1.65}\text{S}_3$ having the smallest deviation. A large composition deviation could give rise to significant concentrations of crystallographic defects such as interstitial atoms, vacancies, and antisites. These defects could act as the recombination centers for the photoexcited charge carriers and thereby making the NCs undesirable for PEC applications.

Electrophoretic Deposition. In order to examine the PEC performance of the $(\text{Cu}_2\text{Sn})_x\text{Zn}_{3(1-x)}\text{S}_3$ NCs for water splitting, we adopted a simple EPD method to prepare NC films. It should be noted that before the EPD process is performed, any excess OLE ligands should be removed by further washing with isopropyl alcohol to make sure that the NCs can be charged and deposited on the FTO substrate. However, the OLE ligands cannot be completely removed from the surface of the NCs or they can precipitate in the solution and electrophoretic deposition will not be successful. The schematic illustration of the EPD process is shown in Figure 7a. Under dc voltage, the negatively and positively charged NCs move to oppositely charged electrodes and deposition of the $(\text{Cu}_2\text{Sn})_x\text{Zn}_{3(1-x)}\text{S}_3$ NCs on both electrodes has been achieved. Similar results have already been reported for TiO_2 , CdSe , and Eu_2O_3 films prepared by the EPD method.^{40,55,56} The $(\text{Cu}_2\text{Sn})_x\text{Zn}_{3(1-x)}\text{S}_3$ films on both electrodes show nearly the same absorption spectra and photocurrents (Figure S1 of the Supporting Information). It is noticed that the $(\text{Cu}_2\text{Sn})_{0.1}\text{Zn}_{2.7}\text{S}_3$ ($x = 0.10$) and $(\text{Cu}_2\text{Sn})_{0.05}\text{Zn}_{2.85}\text{S}_3$ ($x = 0.05$) NC films could not be prepared by the EPD method, possibly due to their instability.³⁹

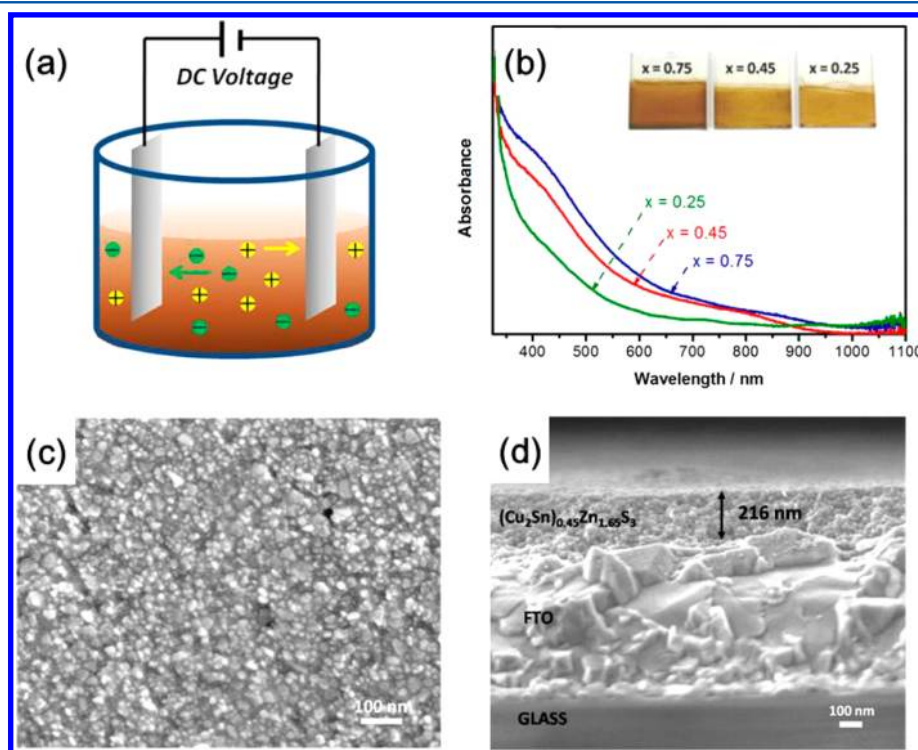


Figure 7. (a) Illustration of the electrophoretic deposition for $(\text{Cu}_2\text{Sn})_x\text{Zn}_{3(1-x)}\text{S}_3$ film preparation. (b) UV-vis absorption spectra of the $(\text{Cu}_2\text{Sn})_x\text{Zn}_{3(1-x)}\text{S}_3$ films with different x values ($x = 0.25$, 0.45 , and 0.75). The inset shows the photographs of different $(\text{Cu}_2\text{Sn})_x\text{Zn}_{3(1-x)}\text{S}_3$ films. FESEM images of the $(\text{Cu}_2\text{Sn})_{0.45}\text{Zn}_{1.65}\text{S}_3$ ($x = 0.45$) film with three deposition cycles: (c) a top view and (d) a side view.

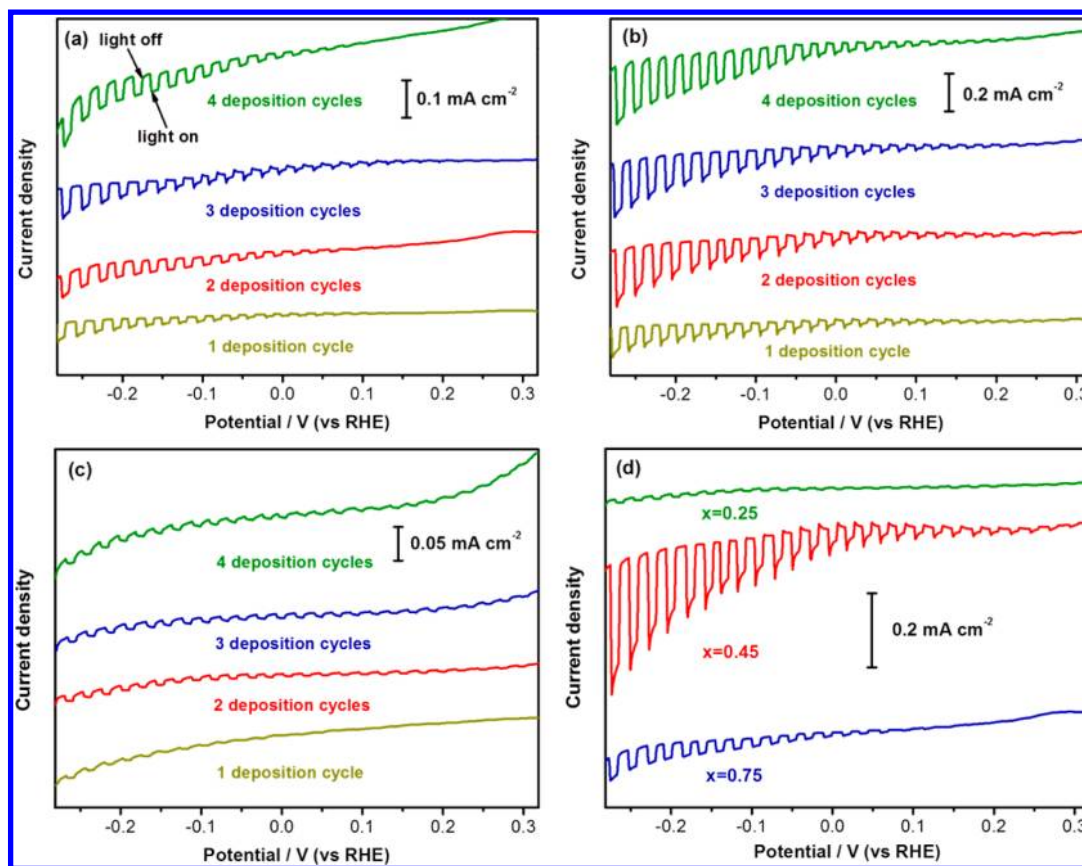


Figure 8. Current–potential curves of the prepared $(\text{Cu}_2\text{Sn})_x\text{Zn}_{3(1-x)}\text{S}_3$ ($0.25 \leq x \leq 0.75$) films with varying deposition cycles and x values: (a) $x = 0.75$, (b) $x = 0.45$, and (c) $x = 0.25$. Three different films with two deposition cycles are shown in (d) for comparison. The PEC measurements were carried out in the 0.1 M Na_2SO_4 solution (pH ~ 3) with a mechanical chopper to turn on/off illumination (AM 1.5).

Figure 7b presents UV–vis absorption spectra of the $(\text{Cu}_2\text{Sn})_x\text{Zn}_{3(1-x)}\text{S}_3$ ($0.25 \leq x \leq 0.75$) films. Similar absorption between films and colloidal solutions indicates that $(\text{Cu}_2\text{Sn})_x\text{Zn}_{3(1-x)}\text{S}_3$ NCs are successfully deposited onto the FTO substrates. The digital photograph of the prepared electrodes (inset of Figure 7b) shows that the films become darker upon increasing the x value. The thickness of the film was controlled by increasing the number of deposition cycles performed, and it was observed that the optical absorption increased as the film thickness increased (Figure S2 of the Supporting Information).

The morphology of the $(\text{Cu}_2\text{Sn})_{0.45}\text{Zn}_{1.65}\text{S}_3$ ($x = 0.45$) film prepared with three deposition cycles was characterized by FESEM shown in Figure 7c and 7d. The top view image shows that $(\text{Cu}_2\text{Sn})_{0.45}\text{Zn}_{1.65}\text{S}_3$ NCs are densely deposited and evenly distributed throughout the FTO surface without any cracks (Figure 7c). The side view in Figure 7d also shows close-packed NCs adhered to the FTO substrate which could facilitate charge transfer from the NC film to the conductive substrate. Under the FESEM, the film thickness is determined to be ~ 216 nm after three deposition cycles. The $(\text{Cu}_2\text{Sn})_{0.45}\text{Zn}_{1.65}\text{S}_3$ NCs have a size of ~ 12 nm (Table 1); therefore, three deposition cycles finally resulted in an accumulation of ~ 18 layers. As shown in Supporting Information Figure S3, the CZTS ($x = 0.75$) and $(\text{Cu}_2\text{Sn})_{0.25}\text{Zn}_{2.25}\text{S}_3$ ($x = 0.25$) films with three deposition cycles, respectively, have a thickness of 236 and 228 nm, close to that of $(\text{Cu}_2\text{Sn})_{0.45}\text{Zn}_{1.65}\text{S}_3$ films with three deposition cycles. Meanwhile, the $(\text{Cu}_2\text{Sn})_{0.45}\text{Zn}_{1.65}\text{S}_3$ film with two deposition cycles is thinner with 162 nm, indicating that

the film thickness can be successfully adjusted by the number of deposition cycles.

Photoelectrochemical Measurements. Figure 8 shows the current–potential curves of different films prepared by EPD in 0.1 M Na_2SO_4 solution under chopped illumination. It is found that $(\text{Cu}_2\text{Sn})_x\text{Zn}_{3(1-x)}\text{S}_3$ films exhibit p-type semiconductor character. All the films generate cathodic photocurrents which gradually increase as the applied potential becomes more negative. As displayed in Figure 8a, the CZTS film with two deposition cycles (red) has an improved photocurrent compared to the film with only one deposition cycle (yellow), but further increase in deposited NCs does not enhance the photocurrent. Similar results are also found in the $(\text{Cu}_2\text{Sn})_x\text{Zn}_{3(1-x)}\text{S}_3$ films with x values of 0.45 and 0.25 (Figures 8b and 8c). Hence, the thickness of $(\text{Cu}_2\text{Sn})_x\text{Zn}_{3(1-x)}\text{S}_3$ films after two deposition cycles was found to be optimal. The photoexcited electrons and holes can be easily transferred to the electrolyte and FTO substrate when there are only a few NC layers. The photocurrent is considered to be mainly limited by the film absorption which can be improved by depositing more NCs on the substrate. On the other hand, as more NCs are deposited, more crystal boundaries are formed and the distance the charge carriers must travel to reach the FTO or electrolyte is longer. Both of these factors could lead to increased charge carrier recombination, and in this way a thicker film would not be beneficial to increasing the photocurrent. Therefore, a balance of absorption and film thickness must be achieved. From this study we have

found that the photocurrents of the films with three or four deposition cycles were not further improved (Figure 8).

In Figure 8d, the photocurrents of three different $(\text{Cu}_2\text{Sn})_x\text{Zn}_{3(1-x)}\text{S}_3$ films with two deposition cycles are compared. The $(\text{Cu}_2\text{Sn})_{0.45}\text{Zn}_{1.65}\text{S}_3$ ($x = 0.45$) film has the highest photocurrent under AM 1.5 illumination. It was reported that the photocurrent increases along with decreasing Zn content for $\text{Cd}_x\text{Zn}_{(1-x)}\text{S}$ due to the decreasing band gap.^{57,58} In our quaternary NC films both CZTS and $(\text{Cu}_2\text{Sn})_{0.45}\text{Zn}_{1.65}\text{S}_3$ ($x = 0.45$) have higher photocurrents than that of $(\text{Cu}_2\text{Sn})_{0.25}\text{Zn}_{2.25}\text{S}_3$ ($x = 0.25$). Instead of CZTS, the $(\text{Cu}_2\text{Sn})_{0.45}\text{Zn}_{1.65}\text{S}_3$ ($x = 0.45$) has the best performance among the three NC films prepared. It is likely that there are factors other than the band gap affecting the photocurrent of the prepared films. The onset potentials of CZTS ($x = 0.75$), $(\text{Cu}_2\text{Sn})_{0.45}\text{Zn}_{1.65}\text{S}_3$ ($x = 0.45$), and $(\text{Cu}_2\text{Sn})_{0.25}\text{Zn}_{2.25}\text{S}_3$ ($x = 0.25$) are determined to be ca. +0.13, +0.24, and +0.33 V vs RHE from Figure 8 and Supporting Information Figure S4. In semiconductor electrodes, the onset potential of the cathodic photocurrent is close to the potential of the valence band edge (E_{VB}). The potential of the conduction band edge (E_{CB}) can be determined by subtracting the band gap (E_{g}) from E_{VB} .³⁷ Through this methodology, the band positions of $(\text{Cu}_2\text{Sn})_x\text{Zn}_{3(1-x)}\text{S}_3$ ($0.25 \leq x \leq 0.75$) can be estimated (Figure S5 in the Supporting Information). Decreasing the x value in $(\text{Cu}_2\text{Sn})_x\text{Zn}_{3(1-x)}\text{S}_3$ ($0.25 \leq x \leq 0.75$) leads to a more positive valence band edge, which is due to the valence band mainly composed of Cu 3d and S 3p orbitals.^{33,38} The more positive valence band will provide larger driving force to transfer the photoexcited holes in the working electrodes to the counter electrode, resulting in more efficient charge separation. Taking both band gap and valence band position into account, the band structure of $(\text{Cu}_2\text{Sn})_{0.45}\text{Zn}_{1.65}\text{S}_3$ ($x = 0.45$) should be the best one for PEC water splitting among the three $(\text{Cu}_2\text{Sn})_x\text{Zn}_{3(1-x)}\text{S}_3$ films.

As shown in Figure 4, with decreasing x value, the morphology of $(\text{Cu}_2\text{Sn})_x\text{Zn}_{3(1-x)}\text{S}_3$ ($0.25 \leq x \leq 0.75$) NCs is varied. Their surface-to-volume ratios can be calculated from the results in Figure 4g by approximately considering the shapes of CZTS ($x = 0.75$) and $(\text{Cu}_2\text{Sn})_x\text{Zn}_{3(1-x)}\text{S}_3$ ($x = 0.45$ and 0.25) NCs as sphere and cylinder. It is found that $(\text{Cu}_2\text{Sn})_{0.45}\text{Zn}_{1.65}\text{S}_3$ NCs have the largest surface-to-volume ratio (Supporting Information Figure S6). Since the photoexcited electrons can transfer to the surface of the $(\text{Cu}_2\text{Sn})_x\text{Zn}_{3(1-x)}\text{S}_3$ film, the larger surface-to-volume ratio of the NCs can improve the surface reaction. Therefore, the morphology of $(\text{Cu}_2\text{Sn})_{0.45}\text{Zn}_{1.65}\text{S}_3$ NCs, leading to the highest surface-to-volume ratio, should contribute to the highest photocurrent.

It was reported by Torimoto et al. that the photocurrent and IPCE of Cu–Zn–Sn–S films depend on the Cu/Sn ratio.³⁷ In the present study, the Cu/Sn ratios for the synthesis of $(\text{Cu}_2\text{Sn})_x\text{Zn}_{3(1-x)}\text{S}_3$ ($0.25 \leq x \leq 0.75$) samples are all fixed to be 2.0. However, the experimentally obtained Cu/Sn ratios of CZTS ($x = 0.75$), $(\text{Cu}_2\text{Sn})_{0.45}\text{Zn}_{1.65}\text{S}_3$ ($x = 0.45$), and $(\text{Cu}_2\text{Sn})_{0.25}\text{Zn}_{2.25}\text{S}_3$ ($x = 0.25$) are 2.8, 2.2, and 2.8, respectively, calculated from the results in Figure 6a. Compared with the Cu/Sn ratio of 2.2 for $(\text{Cu}_2\text{Sn})_{0.45}\text{Zn}_{1.65}\text{S}_3$, the much larger Cu/Sn ratios of 2.8 for CZTS and $(\text{Cu}_2\text{Sn})_{0.25}\text{Zn}_{2.25}\text{S}_3$ can lead to additional crystal defects, which will decrease the efficiency of charge separation. On the other hand, as shown in Figure 6, $(\text{Cu}_2\text{Sn})_{0.45}\text{Zn}_{1.65}\text{S}_3$ has the smallest compositional deviation. A large compositional deviation could give rise to significant

concentrations of defects, acting as recombination centers of photoexcited charge carriers. Therefore, both the smallest Cu/Sn deviation and overall smallest compositional deviation of $(\text{Cu}_2\text{Sn})_{0.45}\text{Zn}_{1.65}\text{S}_3$ can contribute to the highest photocurrent. In summary, the highest photocurrent of $(\text{Cu}_2\text{Sn})_{0.45}\text{Zn}_{1.65}\text{S}_3$ ($x = 0.45$) film should be ascribed to its suitable band structure, morphology, and smallest compositional deviation.

In addition to the current–potential performance, the IPCE of the $(\text{Cu}_2\text{Sn})_{0.45}\text{Zn}_{1.65}\text{S}_3$ ($x = 0.45$) film with two deposition cycles was measured under irradiation of monochromatic light with varying wavelength (400–900 nm) under an applied potential of -0.28 V vs RHE. As shown in Figure 9, the

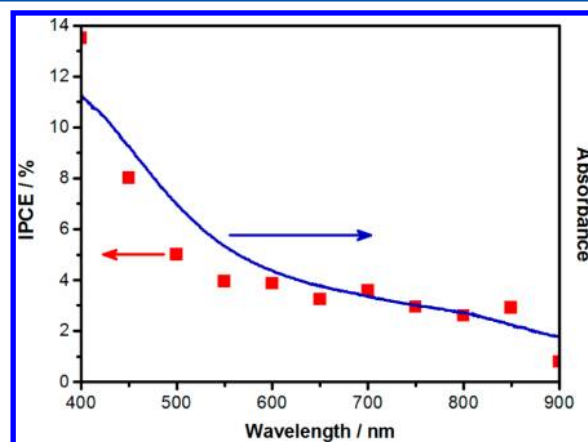


Figure 9. IPCE (red dots) and absorption (blue curve) spectrum of the $(\text{Cu}_2\text{Sn})_{0.45}\text{Zn}_{1.65}\text{S}_3$ ($x = 0.45$) film with two deposition cycles. The IPCE was measured at -0.28 V vs RHE in 0.1 M Na_2SO_4 solution ($\text{pH} \sim 3$).

obtained IPCE spectrum is consistent with the absorption curve, and it is evident that the photocurrent resulted from photoexcitation of the $(\text{Cu}_2\text{Sn})_{0.45}\text{Zn}_{1.65}\text{S}_3$ NCs. The photocurrent of the $(\text{Cu}_2\text{Sn})_{0.45}\text{Zn}_{1.65}\text{S}_3$ film is observed in the whole visible light region, underlining the advantage of narrow band gap semiconductors for harvesting sunlight. The IPCE gradually declines as the wavelength increases. For example, the observed IPCE is mainly in the range of 3–5%, with an efficiency of 3.9% at 600 nm. This value was 2 orders of magnitude higher than the previous reported IPCE (0.01% at 600 nm under an applied potential of -0.24 V vs RHE) for CZTS photocathodes,³⁰ which is of great importance from the viewpoint of developing efficient photoelectrodes. It is believed that the IPCE of the $(\text{Cu}_2\text{Sn})_{0.45}\text{Zn}_{1.65}\text{S}_3$ photocathode is still limited by a large number of crystallographic defects acting as recombination centers leading to lower efficiencies of the interfacial charge transfer processes.

CONCLUSIONS

A series of $(\text{Cu}_2\text{Sn})_x\text{Zn}_{3(1-x)}\text{S}_3$ ($0 \leq x \leq 0.75$) NCs with tunable optical band gaps were synthesized in this study. With decreasing x values from 0.75 to 0.10, the $(\text{Cu}_2\text{Sn})_x\text{Zn}_{3(1-x)}\text{S}_3$ NCs undergo a morphology transition from spheres, to rods, and then to wires. Based on XRD characterization, CZTS has a pure kesterite structure, and with increasing Zn content kesterite-wurtzite polytypism is formed. To investigate the PEC properties of $(\text{Cu}_2\text{Sn})_x\text{Zn}_{3(1-x)}\text{S}_3$ ($0.25 \leq x \leq 0.75$) under water-splitting conditions, we have fabricated NC films from colloidal solutions by a simple electrophoretic deposition method. Three different $(\text{Cu}_2\text{Sn})_x\text{Zn}_{3(1-x)}\text{S}_3$ films with two

deposition cycles were examined, and the $(\text{Cu}_2\text{Sn})_{0.45}\text{Zn}_{1.65}\text{S}_3$ film with $x = 0.45$ produced the highest photocurrent. The IPCE at 600 nm was 2 orders of magnitude higher compared to previously reported results of CZTS photocathodes. Although the present efficiencies of $(\text{Cu}_2\text{Sn})_x\text{Zn}_{3(1-x)}\text{S}_3$ films are not high enough for practical water-splitting applications, they are still attractive due to the tunable optical properties, cost, and use of sustainable materials. It is expected that further remarkable improvements in efficiency for $(\text{Cu}_2\text{Sn})_x\text{Zn}_{3(1-x)}\text{S}_3$ photocathodes can be achieved by systematic modification of composition, size, and deposition. In summary, the developed simple and low-cost solution-based method for $(\text{Cu}_2\text{Sn})_x\text{Zn}_{3(1-x)}\text{S}_3$ films seems promising for developing photoelectrodes for water splitting.

■ ASSOCIATED CONTENT

Supporting Information

Plots of UV–vis absorption spectra and current–potential curves of the $\text{Cu}_2\text{SnZnS}_4$ films on the different electrodes; absorption spectra of $(\text{Cu}_2\text{Sn})_x\text{Zn}_{3(1-x)}\text{S}_3$ ($0.25 \leq x \leq 0.75$) films with varying numbers of deposition cycles; FESEM side view images of different films; current–potential curves of the prepared $(\text{Cu}_2\text{Sn})_{0.25}\text{Zn}_{2.25}\text{S}_3$ ($x = 0.25$) film with two deposition cycles; band positions of $(\text{Cu}_2\text{Sn})_x\text{Zn}_{3(1-x)}\text{S}_3$ ($0.25 \leq x \leq 0.75$) NCs; surface-to-volume ratios of $(\text{Cu}_2\text{Sn})_x\text{Zn}_{3(1-x)}\text{S}_3$ ($0.25 \leq x \leq 0.75$) NCs. This material is available free of charge via the Internet at <http://pubs.acs.org>.

■ AUTHOR INFORMATION

Corresponding Authors

*E-mail: lj-guo@mail.xjtu.edu.cn. Tel.: +86-29-82663895. Fax: +86-29-82669033.

*E-mail: burda@case.edu. Tel.: +1-216-368-5918. Fax: +1-216-368-3006.

Author Contributions

The manuscript was written through contributions of all authors. All authors have given approval to the final version of the manuscript.

Notes

The authors declare no competing financial interest.

■ ACKNOWLEDGMENTS

C.B. gratefully acknowledges the NSF (CHE-0239688) for funding the project development of quaternary semiconductors and CSC for sending Y.C. to carry out these experiments at CWRU. L.G. is thankful for the financial support from the National Natural Science Foundation of China (Grant No. 51121092) and 863 Program of Department of Sciences and Technology of China (No.2012AA051501). Y.C. is thankful for the grant support by the China Scholarship Council (CSC) for studying at Case Western Reserve University.

■ REFERENCES

- (1) Fujishima, A.; Honda, K. Electrochemical Photolysis of Water at a Semiconductor Electrode. *Nature* **1972**, *238*, 37–38.
- (2) Bard, A. J.; Fox, M. A. Artificial Photosynthesis: Solar Splitting of Water to Hydrogen and Oxygen. *Acc. Chem. Res.* **1995**, *28*, 141–145.
- (3) Grätzel, M. Photoelectrochemical Cells. *Nature* **2001**, *414*, 338–344.
- (4) Walter, M. G.; Warren, E. L.; McKone, J. R.; Boettcher, S. W.; Mi, Q.; Santori, E. A.; Lewis, N. S. Solar Water Splitting Cells. *Chem. Rev.* **2010**, *110*, 6446–6473.
- (5) Lin, Y. J.; Yuan, G. B.; Liu, R.; Zhou, S.; Sheehan, S. W.; Wang, D. W. Semiconductor Nanostructure-Based Photoelectrochemical Water Splitting: A Brief Review. *Chem. Phys. Lett.* **2011**, *507*, 209–215.
- (6) Kronawitter, C. X.; Vayssieres, L.; Shen, S.; Guo, L.; Wheeler, D. A.; Zhang, J. Z.; Antoun, B. R.; Mao, S. S. A Perspective on Solar-Driven Water Splitting with All-Oxide Hetero-Nanostructures. *Energy Environ. Sci.* **2011**, *4*, 3889–3899.
- (7) Tachibana, Y.; Vayssieres, L.; Durrant, J. R. Artificial Photosynthesis for Solar Water-Splitting. *Nat. Photonics* **2012**, *6*, 511–518.
- (8) Khaselev, O.; Turner, J. A. A Monolithic Photovoltaic–Photoelectrochemical Device for Hydrogen Production via Water Splitting. *Science* **1998**, *280*, 425–427.
- (9) Licht, S.; Wang, B.; Mukerji, S.; Soga, T.; Umeno, M.; Tributsch, H. Efficient Solar Water Splitting, Exemplified by RuO_2 -Catalyzed AlGaAs/Si Photoelectrolysis. *J. Phys. Chem. B* **2000**, *104*, 8920–8924.
- (10) Zhang, J.; Bang, J. H.; Tang, C.; Kamat, P. V. Tailored TiO_2 – SrTiO_3 Heterostructure Nanotube Arrays for Improved Photoelectrochemical Performance. *ACS Nano* **2010**, *4*, 387–395.
- (11) Su, J.; Feng, X.; Sloppy, J. D.; Guo, L.; Grimes, C. A. Vertically Aligned WO_3 Nanowire Arrays Grown Directly on Transparent Conducting Oxide Coated Glass: Synthesis and Photoelectrochemical Properties. *Nano Lett.* **2011**, *11*, 203–208.
- (12) Chen, X. Q.; Ye, J. H.; Ouyang, S. X.; Kako, T.; Li, Z. S.; Zou, Z. G. Enhanced Incident Photon-to-Electron Conversion Efficiency of Tungsten Trioxide Photo Anodes Based on 3D-Photonic Crystal Design. *ACS Nano* **2011**, *5*, 4310–4318.
- (13) Formal, F. L.; Grätzel, M.; Sivula, K. Controlling Photoactivity in Ultrathin Hematite Films for Solar Water-Splitting. *Adv. Funct. Mater.* **2010**, *20*, 1099–1107.
- (14) Sayama, K.; Nomura, A.; Arai, T.; Sugita, T.; Abe, R.; Yanagida, M.; Oi, T.; Iwasaki, Y.; Abe, Y.; Sugihara, H. Photoelectrochemical Decomposition of Water into H_2 and O_2 on Porous BiVO_4 Thin-Film Electrodes under Visible Light and Significant Effect of Ag Ion Treatment. *J. Phys. Chem. B* **2006**, *110*, 11352–11360.
- (15) Woodhouse, M.; Herman, G. S.; Parkinson, B. A. Combinatorial Approach to Identification of Catalysts for the Photoelectrolysis of Water. *Chem. Mater.* **2005**, *17*, 4318–4324.
- (16) Woodhouse, M.; Parkinson, B. A. Combinatorial Discovery and Optimization of a Complex Oxide with Water Photoelectrolysis Activity. *Chem. Mater.* **2008**, *20*, 2495–2502.
- (17) Sebastian, P. J.; Calixto, M. E.; Bhattacharya, R. N.; Noufi, R. Compositional and Optoelectronic Properties of CIS and CIGS Thin Films Formed by Electrodeposition. *Sol. Energy Mater. Sol. Cells* **1999**, *59*, 125–135.
- (18) Ikeda, S.; Nakamura, T.; Lee, S.; Yagi, T.; Harada, T.; Minegishi, T.; Matsumura, M. Photoreduction of Water by Using Modified CuInS_2 Electrodes. *ChemSusChem* **2011**, *4*, 262–268.
- (19) Valderrama, R. C.; Sebastian, P. J.; Enriquez, J. P.; Gamboa, S. A. Photoelectrochemical Characterization of CIGS Thin Films for Hydrogen Production. *Sol. Energy Mater. Sol. Cells* **2005**, *88*, 145–155.
- (20) Kim, J.; Minegishi, T.; Kobota, J.; Domen, K. Enhanced Photoelectrochemical Properties of CuGa_3Se_5 Thin Films for Water Splitting by the Hydrogen Mediated Co-Evaporation Method. *Energy Environ. Sci.* **2012**, *5*, 6368–6374.
- (21) Marsen, B.; Cole, B.; Miller, E. L. Photoelectrolysis of Water Using Thin Copper Gallium Diselenide Electrodes. *Sol. Energy Mater. Sol. Cells* **2008**, *92*, 1054–1058.
- (22) Steinhagen, C.; Panthani, M. G.; Akhavan, V.; Goodfellow, B.; Koo, B.; Korgel, B. A. Synthesis of $\text{Cu}_2\text{ZnSnS}_4$ Nanocrystals for Use in Low-Cost Photovoltaics. *J. Am. Chem. Soc.* **2009**, *131*, 12554–12555.
- (23) Guo, Q.; Hillhouse, H. W.; Agrawal, R. Synthesis of $\text{Cu}_2\text{ZnSnS}_4$ Nanocrystal Ink and Its Use for Solar Cells. *J. Am. Chem. Soc.* **2009**, *131*, 11672–11673.
- (24) Ahmed, S.; Reuter, K. B.; Gunawan, O.; Guo, L.; Romankiw, L. T.; Deligianni, H. A High Efficiency Electrodeposited $\text{Cu}_2\text{ZnSnS}_4$ Solar Cell. *Adv. Energy Mater.* **2012**, *2*, 253–259.
- (25) Shin, B.; Gunawan, O.; Zhu, Y.; Bojarczuk, N.; Chey, S. J.; Guha, S. Thin Film Solar Cell with 8.4% Power Conversion Efficiency

Using an Earth-Abundant $\text{Cu}_2\text{ZnSnS}_4$ Absorber. *Prog. Photovoltaics* **2013**, *21*, 72–76.

(26) Todorov, T. K.; Tang, J.; Bag, S.; Gunawan, O.; Gokmen, T.; Zhu, Y.; Mitzi, D. B. Beyond 11% Efficiency: Characteristics of State-of-the-Art $\text{Cu}_2\text{ZnSn}(\text{S},\text{Se})_4$ Solar Cells. *Adv. Energy Mater.* **2013**, *3*, 34–38.

(27) Kameyama, T.; Osaki, T.; Okazaki, K.-i.; Shibayama, T.; Kudo, A.; Kuwabata, S.; Torimoto, T. Preparation and Photoelectrochemical Properties of Densely Immobilized $\text{Cu}_2\text{ZnSnS}_4$ Nanoparticle Films. *J. Mater. Chem.* **2010**, *20*, 5319–5324.

(28) Riha, S. C.; Fredrick, S. J.; Sambur, J. B.; Liu, Y.; Prieto, A. L.; Parkinson, B. A. Photoelectrochemical Characterization of Nanocrystalline Thin-Film $\text{Cu}_2\text{ZnSnS}_4$ Photocathodes. *ACS Appl. Mater. Interfaces* **2011**, *3*, 58–66.

(29) Scragg, J. J.; Dale, P. J.; Peter, L. M. Towards Sustainable Materials for Solar Energy Conversion: Preparation and Photoelectrochemical Characterization of $\text{Cu}_2\text{ZnSnS}_4$. *Electrochem. Commun.* **2008**, *10*, 639–642.

(30) Yokoyama, D.; Minegishi, T.; Jimbo, K.; Hisatomi, T.; Ma, G.; Katayama, M.; Kubota, J.; Katagiri, H.; Domen, K. H_2 Evolution from Water on Modified $\text{Cu}_2\text{ZnSnS}_4$ Photoelectrode under Solar Light. *Appl. Phys. Express* **2010**, *3*, 101202(1–3).

(31) Ma, G.; Minegishi, T.; Yokoyama, D.; Kubota, J.; Domen, K. Photoelectrochemical Hydrogen Production on $\text{Cu}_2\text{ZnSnS}_4/\text{Mo}$ -Mesh Thin-Film Electrodes Prepared by Electroplating. *Chem. Phys. Lett.* **2011**, *501*, 619–622.

(32) Rovelli, L.; Tilley, S. D.; Sivula, K. Optimization and Stabilization of Electrodeposited $\text{Cu}_2\text{ZnSnS}_4$ Photocathodes for Solar Water Reduction. *ACS Appl. Mater. Interfaces* **2013**, *5*, 8018–8024.

(33) Tsuji, I.; Shimodaira, Y.; Kato, H.; Kobayashi, H.; Kudo, A. Novel Stannite-Type Complex Sulfide Photocatalysts $\text{A}^{\text{I}}_2\text{Zn-A}^{\text{IV}}\text{S}_4$ ($\text{A}^{\text{I}} = \text{Cu}$ and Ag ; $\text{A}^{\text{IV}} = \text{Sn}$ and Ge) for Hydrogen Evolution under Visible-Light Irradiation. *Chem. Mater.* **2010**, *22*, 1402–1409.

(34) Ford, G. M.; Guo, Q. J.; Agrawal, R.; Hillhouse, H. W. Earth Abundant Element $\text{Cu}_2\text{Zn}(\text{Sn}_{1-x}\text{Ge}_x)\text{S}_4$ Nanocrystals for Tunable Band Gap Solar Cells: 6.8% Efficient Device Fabrication. *Chem. Mater.* **2011**, *23*, 2626–2629.

(35) Dai, P. C.; Shen, X. N.; Lin, Z. J.; Feng, Z. Y.; Xu, H.; Zhan, J. H. Band-gap Tunable $(\text{Cu}_2\text{Sn})_{x/3}\text{Zn}_{1-x}\text{S}$ Nanoparticles for Solar Cells. *Chem. Commun.* **2010**, *46*, 5749–5751.

(36) Liu, Q.; Zhao, Z.; Lin, Y.; Guo, P.; Li, S.; Pan, D.; Ji, X. Alloyed $(\text{ZnS})_x(\text{Cu}_2\text{SnS}_3)_{1-x}$ and $(\text{CuInS}_2)_x(\text{Cu}_2\text{SnS}_3)_{1-x}$ Nanocrystals with Arbitrary Composition and Broad Tunable Band Gaps. *Chem. Commun.* **2011**, *47*, 964–966.

(37) Nishi, H.; Kuwabata, S.; Torimoto, T. Composition-Dependent Photoelectrochemical Properties of Nonstoichiometric $\text{Cu}_2\text{ZnSnS}_4$ Nanoparticles. *J. Phys. Chem. C* **2013**, *117*, 21055–21063.

(38) Walsh, A.; Chen, S.; Wei, S. H.; Gong, X. G. Kesterite Thin-Film Solar Cells: Advances in Materials Modelling of $\text{Cu}_2\text{ZnSnS}_4$. *Adv. Energy Mater.* **2012**, *2*, 400–409.

(39) Besra, L.; Liu, M. A Review on Fundamentals and Applications of Electrophoretic Deposition (EPD). *Prog. Mater. Sci.* **2007**, *52*, 1–61.

(40) Islam, M. A.; Xia, Y. Q.; Telesca, D. A.; Steigerwald, M. L.; Herman, I. P. Controlled Electrophoretic Deposition of Smooth and Robust Films of CdSe Nanocrystals. *Chem. Mater.* **2004**, *16*, 49–54.

(41) Bang, J. H.; Kamat, P. V. CdSe Quantum Dot-Fullerene Hybrid Nanocomposite for Solar Energy Conversion: Electron Transfer and Photoelectrochemistry. *ACS Nano* **2011**, *5*, 9421–9427.

(42) Grinis, L.; Dor, S.; Ofir, A.; Zaban, A. Electrophoretic Deposition and Compression of Titania Nanoparticle Films for Dye-Sensitized Solar Cells. *J. Photochem. Photobiol., A* **2008**, *198*, 52–59.

(43) Jo, W.; Jang, J.; Kong, K.; Kang, H.; Kim, J.; Jun, H.; Parmar, K.; Lee, J. Phosphate Doping into Monoclinic BiVO_4 for Enhanced Photoelectrochemical Water Oxidation Activity. *Angew. Chem., Int. Ed.* **2012**, *51*, 3147–3151.

(44) Kornhuber, K.; Kavalakkatt, J.; Lin, X.; Ennaoui, A.; Lux-Steiner, M. C. In Situ Monitoring of Electrophoretic Deposition of $\text{Cu}_2\text{ZnSnS}_4$ Nanocrystals. *RSC Adv.* **2013**, *3*, 5845–5850.

(45) Mao, B.; Chuang, C. H.; Wang, J.; Burda, C. Synthesis and Photophysical Properties of Ternary I–III–VI AgInS_2 Nanocrystals: Intrinsic versus Surface States. *J. Phys. Chem. C* **2011**, *115*, 8945–8954.

(46) Chen, Y.; Guo, L. Highly Efficient Visible-Light-Driven Photocatalytic Hydrogen Production from Water Using $\text{Cd}_{0.5}\text{Zn}_{0.5}\text{S}/\text{TNTs}$ (Titanate Nanotubes) Nanocomposites without Noble Metals. *J. Mater. Chem.* **2012**, *22*, 7507–7514.

(47) Chen, S. Y.; Gong, X. G.; Walsh, A.; Wei, S. H. Electronic Structure and Stability of Quaternary Chalcogenide Semiconductors Derived from Cation Cross-Substitution of II–VI and I–III–VI₂ Compounds. *Phys. Rev. B* **2009**, *79*, 165211(1–10).

(48) Deng, Z.; Qi, J.; Zhang, Y.; Liao, Q.; Huang, Y. Growth Mechanism and Optical Properties of ZnS Nanotetrapods. *Nanotechnology* **2007**, *18*, 475603(1–4).

(49) Aihara, N.; Araki, H.; Takeuchi, A.; Jimbo, K.; Katagiri, H. Fabrication of Cu_2SnS_3 Thin Films by Sulfurization of Evaporated Cu–Sn Precursors for Solar Cells. *Phys. Status Solidi C* **2013**, *10*, 1086–1092.

(50) Wang, Y.-H. A.; Zhang, X.; Bao, N.; Lin, B.; Gupta, A. Synthesis of Shape-Controlled Monodisperse Wurtzite $\text{CuIn}_{1-x}\text{Ga}_x\text{S}_2$ Semiconductor Nanocrystals with Tunable Band Gap. *J. Am. Chem. Soc.* **2011**, *133*, 11072–11075.

(51) Lu, X.; Zhuang, Z.; Peng, Q.; Li, Y. Wurtzite $\text{Cu}_2\text{ZnSnS}_4$ Nanocrystals: A Novel Quaternary Semiconductor. *Chem. Commun.* **2011**, *47*, 3141–3143.

(52) Zhao, Y.; Zhang, Y.; Zhu, H.; Hadjipanayis, G. C.; Xiao, J. Q. Low-Temperature Synthesis of Hexagonal (Wurtzite) ZnS Nanocrystals. *J. Am. Chem. Soc.* **2004**, *126*, 6874–6875.

(53) Singh, A.; Geaney, H.; Laffir, F.; Ryan, K. M. Colloidal Synthesis of Wurtzite $\text{Cu}_2\text{ZnSnS}_4$ Nanorods and Their Perpendicular Assembly. *J. Am. Chem. Soc.* **2012**, *134*, 2910–2913.

(54) Khare, A.; Wills, A. W.; Ammerman, L. M.; Norris, D. J.; Aydil, E. S. Size Control and Quantum Confinement in $\text{Cu}_2\text{ZnSnS}_4$ Nanocrystals. *Chem. Commun.* **2011**, *47*, 11721–11723.

(55) Gonzalo-Juan, I.; Krejci, A. J.; Dickerson, J. H. Toward Dynamic Control over TiO_2 Nanocrystal Monolayer-by-Monolayer Film Formation by Electrophoretic Deposition in Nonpolar Solvents. *Langmuir* **2012**, *28*, 5295–5301.

(56) Mahajan, S. V.; Dickerson, J. H. Understanding the Growth of Eu_2O_3 Nanocrystal Films Made via Electrophoretic Deposition. *Nanotechnology* **2010**, *21*, 145704(1–9).

(57) Shi, J.; Cui, H. N.; Liang, Z.; Lu, X.; Tong, Y. X.; Su, C.; Liu, H. The Roles of Defect States in Photoelectric and Photocatalytic Processes for $\text{Zn}_x\text{Cd}_{1-x}\text{S}$. *Energy Environ. Sci.* **2011**, *4*, 466–470.

(58) Li, M. T.; Jiang, J. G.; Guo, L. J. Synthesis, Characterization, and Photoelectrochemical Study of $\text{Cd}_{1-x}\text{Zn}_x\text{S}$ Solid Solution Thin Films Deposited by Spray Pyrolysis for Water Splitting. *Int. J. Hydrogen Energy* **2010**, *35*, 7036–7042.